

Structural Optimization of Composite Blades for Wind and Hydrokinetic Turbines

Danny Sale^{*†}, Alberto Aliseda^{*}, and Michael Motley^{**}

^{*}Dept. of Mechanical Engineering

^{**}Dept. of Civil & Environmental Engineering

University of Washington

Seattle, Washington, USA

dsale@uw.edu, aaliseda@uw.edu, mrmotley@uw.edu

Ye Li, IEEE Senior Member
National Wind Technology Center
National Renewable Energy Laboratory
Golden, Colorado, USA
ye.li@nrel.gov

[†] corresponding author

I. INTRODUCTION

In this work we develop a numerical methodology for the structural analysis and optimization of composite blades for wind and hydrokinetic turbines. While the methodology presented here is equally applicable to the design of wind turbines, this paper focuses on its application to hydrokinetic turbines.

First, we derive a structural mechanics model which is based upon a combination of classical lamination theory with an Euler-Bernoulli and shear flow theory applied to composite beams. The development of this simplified structural model was motivated by the need for an accurate and computationally efficient method that is suitable for parametric design and optimization studies of composite blades. An important characteristic of this structural model is its ability to handle complex geometric shapes and isotropic or anisotropic composite layups.

After validating our simplified structural model, we formulate a structural optimization problem which determines an optimal layout of composite materials within the blade. For a specified design load, the objective of the structural optimization is to minimize the blade's mass while satisfying constraints on maximum allowable stress, blade tip deflection, buckling, and placement of blade natural frequencies. We demonstrate this optimization methodology to produce a hypothetical design for a composite blade of a utility-scale horizontal-axis hydrokinetic turbine operating in the Admiralty Inlet of Puget Sound, Washington, USA. This particular blade design uses a combination of E-glass, carbon fiber, and foam composite materials. In solving this structural optimization problem, we compare the efficiency of two deterministic optimization algorithms (gradient search and pattern search) and a stochastic particle swarm algorithm.

Finally, we quantify the effects that uncertain material properties can have on the structural performance of composite blades and provide an estimate of the probability of structural failure for a given design. Studying the relationships between material properties and structural performance provides further insights into creating higher-performance, more reliable, and cheaper turbine blades.

II. STRUCTURAL MECHANICS MODEL

Current state of the art approaches for the structural analysis of composite blades consist of finite element methods (FEM) which can accurately account for complex geometric shapes, 3D and non-linear behavior, and extensive use of composite materials. However, FEM approaches become impractical for use in the preliminary design stages (where hundreds or potentially thousands of alternative designs may be evaluated) due to the labor intensive task of generating accurate meshes and higher computational cost. In the preliminary design stages it becomes important to develop simplified and computationally efficient, yet accurate, numerical models in order to perform parametric design and optimization studies. The following sections summarize the development and validation of such a simplified structural model tailored towards composite rotor blades.

A. TECHNICAL APPROACH

We have developed an open source structural analysis code, Co-Blade [1], which is utilized to perform structural design of composite blades. The underlying theory for structural analysis in the Co-Blade code is based upon a combination of classical lamination theory (CLT) with an Euler-Bernoulli and shear flow theory applied to composite beams. In this model, the turbine blade is represented as an Euler-Bernoulli cantilever beam which undergoes flapwise and edgewise bending, axial deflection, and elastic twist. In addition to hydrodynamic loads, the body forces from self-weight, buoyancy, and centrifugal forces also contribute to deflection of the beam.

Equations (2.1-6) are the linear differential equations of equilibrium for a cantilever beam, which give the shear forces (V) and bending moments (M) resultant from aerodynamic forces (p_a) and aerodynamic moments (q_a), self-weight and buoyancy forces (p_w), and centrifugal forces (p_c). In this analysis, we denote the aerodynamic center (x_{ac}, y_{ac}) as the point where the aerodynamic loads are applied, and the body forces act at the center of mass (x_{cm}, y_{cm}). Additional coupling between bending, extension, and torsion arise by accounting for offsets of the elastic axis, centroidal axis, and inertial axis, as illustrated in Figure 1. Axial loads acting at points offset from the tension center (x_{tc}, y_{tc}) will introduce additional bending moments (M_x, M_y),

and shear forces acting at points offset from the shear center (x_{SC}, y_{SC}) will introduce additional twisting of the blade (Φ_Z) .

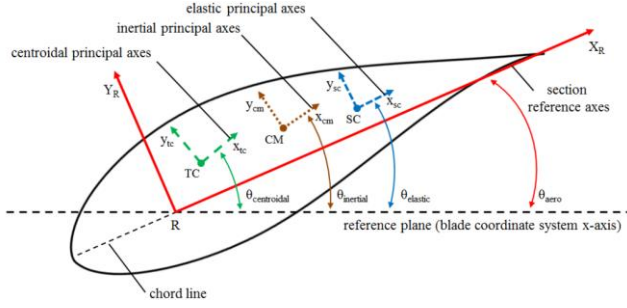


Figure 1. Orientation of the different axes within each cross section of the blade.

$$\frac{dV_x}{dz} = -(p_{x_a} + p_{x_w} + p_{x_c}) \quad (2.1)$$

$$\frac{dV_y}{dz} = -(p_{y_a} + p_{y_w} + p_{y_c}) \quad (2.2)$$

$$\frac{dV_z}{dz} = -(p_{z_w} + p_{z_c}) \quad (2.3)$$

$$\frac{dM_x}{dz} = V_y - (p_{z_w} + p_{z_c})(y_{cm} - y_{tc}) \quad (2.4)$$

$$\frac{dM_y}{dz} = -V_x + (p_{z_w} + p_{z_c})(x_{cm} - x_{tc}) \quad (2.5)$$

$$\begin{aligned} \frac{dM_z}{dz} = & -q_{z_a} - p_{y_a}(x_{ac} - x_{sc}) \\ & - (p_{y_w} + p_{y_c})(x_{cm} - x_{sc}) \\ & + p_{x_a}(y_{ac} - y_{sc}) \\ & + (p_{x_w} + p_{x_c})(y_{cm} - y_{sc}) \end{aligned} \quad (2.6)$$

The beam cross sections are assumed to be thin-walled, closed, and single- or multi-cellular. The periphery of each beam cross section is discretized as a connection of flat composite laminates. The mechanical properties of the composite laminates which discretize each cross section are computed using CLT. Although each laminate is actually an assembly of multiple fibrous composite materials (where each layer can have different constitutive properties), CLT is used to calculate a set of “effective” mechanical properties which allows a multi-layered composite plate to be treated as a single structural element [2]. Therefore, the beam cross sections are composed of discrete sections of homogenous material (as illustrated in Figure 2), where each discrete portion of the composite beam is characterized by effective mechanical properties computed via CLT.

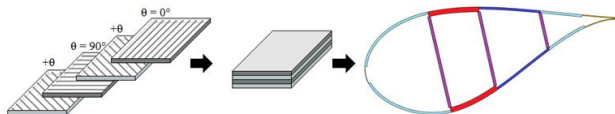


Figure 2. The blade cross sections are discretized as a connection of composite laminated plates.

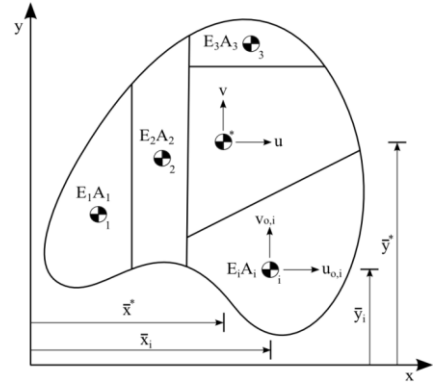


Figure 3. Example of a cross section for a heterogeneous composite beam.

For a heterogeneous composite beam, the modulus weighted section properties are defined as

$$A^* = \int_A \frac{E}{E_{ref}} dA = \frac{1}{E_{ref}} \sum_{i=1}^n E_i A_i \quad (2.7)$$

$$x_c^* = \frac{1}{A^*} \int_A \frac{E}{E_{ref}} x dA = \frac{1}{E_{ref} A^*} \sum_{i=1}^n E_i A_i x_{c_i} \quad (2.8)$$

$$y_c^* = \frac{1}{A^*} \int_A \frac{E}{E_{ref}} y dA = \frac{1}{E_{ref} A^*} \sum_{i=1}^n E_i A_i y_{c_i} \quad (2.9)$$

$$I_x^* = \int_A \frac{E}{E_{ref}} y^2 dA = \frac{1}{E_{ref}} \sum_{i=1}^n E_i (I_{u_o,i} + A_i y_{c_i}^2) \quad (2.10)$$

$$I_y^* = \int_A \frac{E}{E_{ref}} x^2 dA = \frac{1}{E_{ref}} \sum_{i=1}^n E_i (I_{v_o,i} + A_i x_{c_i}^2) \quad (2.11)$$

$$\begin{aligned} I_{xy}^* &= \int_A \frac{E}{E_{ref}} xy dA \\ &= \frac{1}{E_{ref}} \sum_{i=1}^n E_i (I_{uv_o,i} + A_i x_{c_i} y_{c_i}) \end{aligned} \quad (2.12)$$

where E_i is the Young’s modulus, E_{ref} is a reference modulus, (x_{c_i}, y_{c_i}) denote the geometric centroid of each discrete segment of the cross sections, and (u_o, v_o) denotes the principal axes of each discrete segment. The parallel axis theorem, as in Equations (2.13-15), can be applied to compute the moments of inertia about the other beam axes.

$$I_u^* = I_x^* - A^* (y_c^*)^2 \quad (2.13)$$

$$I_v^* = I_y^* - A^* (x_c^*)^2 \quad (2.14)$$

$$I_{uv}^* = I_{xy}^* - A^* x_c^* y_c^* \quad (2.15)$$

Denoting the axial stiffness as $S = E_{ref} A^*$ and bending stiffness as $H = E_{ref} I$, an uncoupled set of

ODEs to describe the transverse and axial displacements (u_o, v_o, w_o) and twist (Φ_z) of the beam centroidal axis (x_{tc}, y_{tc}) is derived as:

$$\frac{d^2 u_o}{dz^2} = \frac{M_y H_x + M_x H_{xy}}{H_x H_y - H_{xy}^2} \xi_{cf} \quad (2.16)$$

$$\frac{d^2 v_o}{dz^2} = \frac{-M_x H_y - M_y H_{xy}}{H_x H_y - H_{xy}^2} \xi_{cf} \quad (2.17)$$

$$\frac{dw_o}{dz} = \frac{V_z}{S} \quad (2.18)$$

$$H_z \frac{d^2 \Phi_z}{dz^2} = \frac{dM_z}{dz} \quad (2.19)$$

where ξ_{cf} [5,9] is a correction factor which depends on the ratio of moments of inertia between the blade root and tip—this correction factor extends the original beam theory to provide more accurate displacements for tapered cantilever beams. The simplifying assumption of plane cross sections in the Euler-Bernoulli beam model implies that there are only 3 non-negligible stress components: the axial stress σ_{zz} and shear stresses τ_{zx} and τ_{zy} . Furthermore, the shear flow assumption for thin-walled sections implies that shear stress is uniform through the wall thickness, and the only non-vanishing shear stress component becomes τ_{zs} which is the shear stress acting in the s -direction (where s is a curvilinear coordinate tangential to a curve which follows the mid-wall thickness around the cross section periphery). Once the global cross sectional properties of the beam are computed using CLT and the method of Young's modulus weighted properties, we can compute the beam centroidal-axis deflections Eqns. (2.16-19), effective beam axial stress Eqn. (2.20), and effective beam shear stress Eqn. (2.21) under the assumptions for an Euler-Bernoulli beam [3].

$$\sigma_{zz}(x, y) = \frac{E}{E_{ref}} \left[\frac{V_z}{A^*} - \frac{M_y I_u^* + M_x I_{uv}^*}{I_u^* I_v^* - I_{uv}^{*2}} (x - x_c^*) + \frac{M_x I_v^* + M_y I_{uv}^*}{I_u^* I_v^* - I_{uv}^{*2}} (y - y_c^*) \right] \quad (2.20)$$

Shear stress is computed using a shear flow approach, where the shear stress is defined as

$$\tau_{zs}(s) = \frac{f}{t} \quad (2.21)$$

and the shear flow in an open section is defined as

$$\frac{df_o}{ds}(s) = -t \frac{\partial \sigma_{zz}}{\partial z} \quad (2.22)$$

Substituting in the stress relation Eqn. (2.20) and the resultant shear forces and bending moments from Eqns.

(2.1-6), the shear flow around an open section is described by Eqn. (2.26). The first constant on the RHS of Eqn. (2.26) is solved from a continuity boundary condition, and we have also introduced the stiffness first moments Eqns. (2.24-25).

$$A_s(s) = \int_0^s E t ds \quad (2.23)$$

$$Q_x(s) = \int_0^s E t \bar{y} ds \quad (2.24)$$

$$Q_y(s) = \int_0^s E t \bar{x} ds \quad (2.25)$$

$$f_o(s) = f_o(s=0) + \left\{ \frac{p_{zw} + p_{zc}}{S} \right\} A_s(s) + (H_{xy} Q_y(s) - H_y Q_x(s)) \left\{ \frac{V_y - (p_{zw} + p_{zc})(y_{cm} - y_{tc})}{H_x H_y - H_{xy}^2} \right\} + (H_x Q_y(s) - H_{xy} Q_x(s)) \left\{ \frac{-V_x + (p_{zw} + p_{zc})(x_{cm} - x_{tc})}{H_x H_y - H_{xy}^2} \right\} \quad (2.26)$$

When analyzing closed thin-walled sections, it is often convenient to first analyze the corresponding "open" section which corresponds by making one cut per cell of the multi-cellular beam. To enforce continuity, the corresponding relative axial displacement must vanish at a "cut" location in a closed cross section, which implies Eqn. (2.27). The closing shear constant f_c can be solved from the system of equations arising from Eqn. (2.27). The corresponding shear stress in a closed section can then be solved by adding the closing shear constant to the open section shear flow, as in Eqn. (2.28).

$$w_i = \oint_{cell_i} \frac{f_o(s) + f_c}{Gt} ds = 0 \quad (2.27)$$

$$f(s) = f_o(s) + f_c \quad (2.28)$$

The calculation of shear stress τ_{zs} , prediction of shear center and torsional stiffness is based on a modified shear flow theory for thin-walled single/multi-cellular sections [1,3]. Finally, by converting the distribution of effective beam stresses σ_{zz} and τ_{zs} into equivalent in-plane distributed loads on the flat laminates which discretize the cross section periphery (as shown in Figure 4), the lamina-level strains and stresses in the principal fiber directions (ε_{11} , ε_{22} , γ_{12} , σ_{11} , σ_{22} , and τ_{12}) are recovered using CLT.

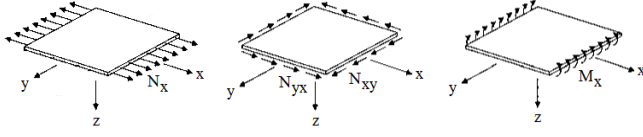


Figure 4. The effective beam stresses from Euler-Bernoulli theory (σ_{zz} and τ_{zs}) are converted into equivalent extensional, shear, and bending loads on a composite laminated plate so that the lamina level stresses and strains (ϵ_{11} , ϵ_{22} , γ_{12} , σ_{11} , σ_{22} , and τ_{12}) can be recovered via CLT.

A linear buckling analysis is implemented to predict the critical buckling stresses [4,5]. In this approach, the top and bottom surfaces of the blade are idealized as curved plates subjected to the combined conditions of compression and shear, while the shear webs are idealized as flat plates subjected to the combined conditions of bending and shear. Figure 5 illustrates the loading conditions used to predict buckling stresses. The plates are idealized as having simply-supported (pinned) boundary conditions on all four sides. Effective mechanical properties of the plates are computed using CLT, and the plates' Young modulus, thickness, curvature, and width all contribute to the prediction of critical buckling stresses. The buckling criteria, R , is defined by Eqn. (2.29), where the exponents depend on boundary conditions [4,5].

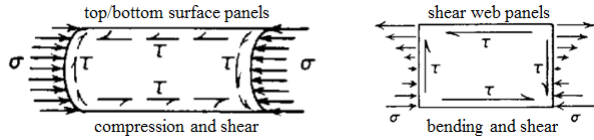


Figure 5. The top and bottom surfaces of the blade are modeled as curved plates subjected to combined compression and shear. The blade shear webs are modeled as flat plates subjected to combined bending and shear.

$$R_b = \left(\frac{\sigma}{\sigma_{buckle}} \right)^\alpha + \left(\frac{\tau}{\tau_{buckle}} \right)^\beta \quad (2.29)$$

The predictions of beam natural frequencies and modal shapes are computed by utilizing the BModes code [6] developed by the National Renewable Energy Laboratory (NREL). In summary, BModes formulates an energy functional and uses Hamilton's principle to derive a set of nonlinear coupled integro-partial differential equations (PDEs) that govern the dynamics of an Euler-Bernoulli beam. BModes discretizes these PDEs using specialized 15 degree-of-freedom finite elements, and then performs an eigenanalysis to obtain the coupled mode shapes and frequencies.

B. VALIDATION

In previous validation studies [1], the structural model in Co-Blade showed excellent agreement for isotropic and prismatic beams with elliptical and

rectangular cross sections for which analytical results could be obtained. To test the capabilities of this method for more complex composite layups, we modeled a cylindrical beam using both Co-Blade and the higher-fidelity ABAQUS finite element code [10]. For three different composite layups ($[0]_8$, $[0/\pm 45/90]_s$, and $[\pm 30]_4$), we find very good agreement between the predicted values for stiffness and beam deflection, as shown in Figure 9.

III. STRUCTURAL OPTIMIZATION

In this study, we develop a structural optimization methodology to design a composite blade for a utility-scale horizontal-axis hydrokinetic turbine operating in the Admiralty Inlet of Puget Sound, Washington, USA. The hydrodynamic design of the 2-bladed, 20-m diameter, 550-kW, variable-speed variable-pitch turbine was created in a previous study using the HARP_Opt turbine optimization code [8]. The structural design load represents a situation in which a large eddy passes through the rotor quicker than the blade pitch control can respond to shed the increased hydrodynamic load. Eddies of this scale result in large stresses on the blades, but they are expected to occur only rarely over the turbine's lifetime [11].

The structural design of the blade uses a combination of E-glass, carbon fiber, and foam composite materials. Mechanical properties of the composite materials are listed in Table 1 [7]. The NCT307-D1-E300 material is a tri-axial E-glass/epoxy composite which is utilized in the "blade-root" section of the blade, as indicated in Figure 7. The "blade-shell" and "web-shell" sections of the blade (see Figure 7) are composed of the NB307-D1-7781-497A bi-axial weave E-glass/epoxy, and the "spar-uni" section of the blade is composed of the NCT307-D1-34-600 unidirectional carbon/epoxy material. The "spar-core", "LEP-core", "TEP-core", and "web-core" sections of the blade are all composed of the Corecell M-Foam M200 material, which is a structural foam developed for marine applications.

The blade is assumed to be a "box-beam" style blade, in which a thick root section transitions into a main spar with two shear webs that run the length of the blade, as illustrated in Figure 6. The leading edge panels (LEP) and trailing edge panels (TEP) are sandwich composite laminates which form the hydrodynamic shape of the blade. As Figures 7 and 8 illustrate, the blade consists of 9 unique laminate schedules with a total of 8 possible materials (where each material can have its own unique properties defined). The thickness of each material along the length of the blade is defined by the linear variation between control points—Figure 8 shows how the material thicknesses in the LEP, TEP, spar cap, and shear webs vary along the length of the blade. The example in Figure 8 shows 5 control points per material

(only 2 control points for the shear webs); however, more or less control points could be used for greater degree-of-freedom or greater computational efficiency.

All laminates are balanced and symmetric, eliminating the possibility for cross-coupled stiffnesses. The ends of the spar caps and shear webs remain fixed at user specified inboard and outboard stations, but the optimization algorithm can vary the chordwise locations of the spar caps and shear webs. The chordwise locations of the spar cap and shear webs are positioned symmetrically about the blade pitch axis.

In order to use continuous design variables, each lamina is modeled as a single ply with continuously variable thickness, as opposed to a stack of multiple plies with discrete thicknesses. The structural design variables (totaling 32 in this case) are:

- chordwise width of the spar cap at the inboard and outboard blade stations
- control point ordinate value for the thickness of the “blade-root” material
- control point ordinate values for the thicknesses of the materials within the LEP, TEP, spar cap, and shear webs along the length of the blade

Table 1. Mechanical properties of the composite materials utilized in the structural design of the blade [7].

	“NCT307-D1-E300” E-Glass	“NB307-D1-7781-497A” E-Glass	“NCT307-D1-34-600” Carbon	“Corecell M-Foam M200” Structural Foam
V_f (%)	47	39	53	n/a
E_{11} (GPa)	35.5	19.2	123	0.21
E_{22} (GPa)	8.33	19.2	8.2	0.21
G_{12} (GPa)	4.12	3.95	4.71	0.098
ν_{12} (-)	0.33	0.13	0.31	0.33
ρ (kg/m ³)	1780	1670	1470	200
$\sigma_{11,fT}$ (MPa)	1005	337	1979	4.29
$\sigma_{11,fC}$ (MPa)	-788	-497	-1000	-4.29
$\sigma_{22,yT}$ (MPa)	51.2	337	59.9	4.29
$\sigma_{22,yC}$ (MPa)	-51.2	-337	-59.9	-4.29
$\tau_{12,y}$ (MPa)	112	115	103	2.95

V_f : fiber volume fraction, E_{11} : principal Young’s modulus, E_{22} : lateral Young’s modulus; G_{12} : shear modulus; ν_{12} : Poisson ratio; ρ : density; $\sigma_{11,fT}$: principal tensile failure stress; $\sigma_{11,fC}$: principal compressive failure stress; $\sigma_{22,yT}$: lateral tensile yielding stress; $\sigma_{22,yC}$: lateral compressive yielding stress; $\tau_{12,y}$: shear yielding stress

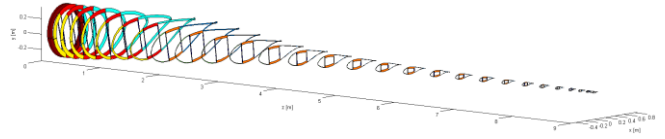


Figure 6. An example of the composite blade model, the colors indicate different laminate stacking orders which corresponds to the illustration of material delineations in Figure 7.

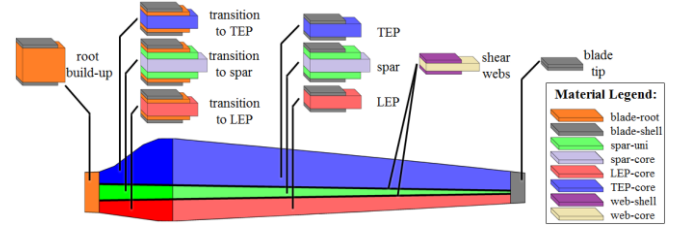


Figure 7. Planform view of the turbine blade configuration used in the optimization study, showing the laminate material schedules in the root build-up, leading edge panel (LEP), spar cap, trailing edge panel (TEP), shear webs, and blade tip.

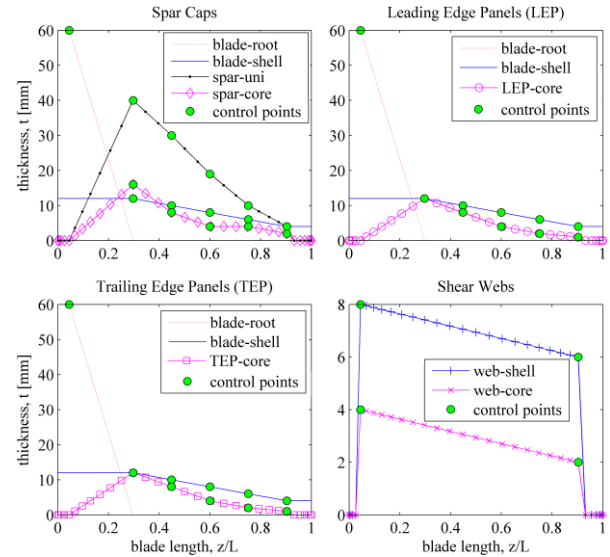


Figure 8. The material thicknesses are defined along the blade length by linear variations between the control points. The laminate material schedule is identical to that illustrated in Figure 7.

The structural objective function Eqn. (3.1) is formulated as an additive penalty function in which the constraints are accounted for by penalty factors p_i . For a specified design load, the objective of the structural optimization is to minimize the blade’s mass while satisfying constraints on maximum allowable stress, blade tip deflection, buckling stress, and placement of blade natural frequencies. The structural objective function $f(\vec{x}_{struct})$ is minimized when the blade mass m_{blade} is minimal and all of the penalty factors, $p_1 - p_8$, are less than unity. Penalty factors $p_1 - p_5$ are greater than 1 if the lamina-level stresses exceed the materials’ maximum allowable stresses. Penalty factor

p_6 is greater than 1 if the effective stresses in a panel (i.e. laminate) have exceeded the critical buckling stresses σ_{buckle} and τ_{buckle} (the exponents α and β are determined from the boundary conditions of the panel [4,5]). Penalty factor p_7 is greater than 1 if the maximum allowable blade tip deflection ($\delta_{tip,allowable}$) has been exceeded. Penalty factor p_8 is greater than 1 if the difference between the blade natural frequency ω_m (for $m = 1 \dots M_{modes}$) and the rotor rotation frequency ω_m is less than the minimum allowable separation $\Delta_{\omega,min}$. The weighting value in Equation 3.1 is set as $w = 2 / m_{blade,initial}$. This choice of w gives greater incentive to minimize the penalty factors (i.e. minimizing stresses) rather than strictly minimizing the blade mass.

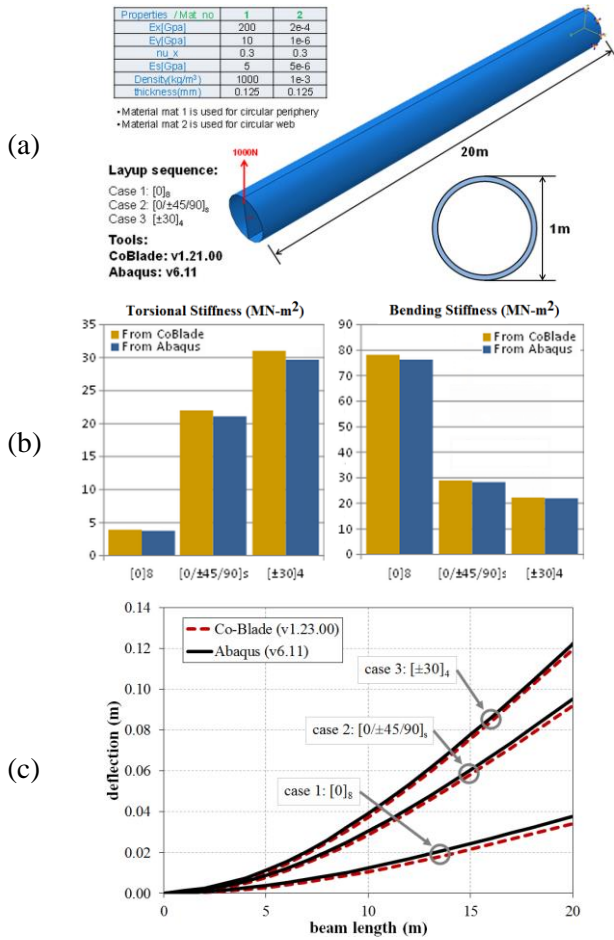


Figure 9. Geometry of a circular composite beam and loading condition (a), computed torsional and bending stiffness (b), and beam deflection (c) [11].

To solve this structural optimization problem, we compared several optimization algorithms. An example of the convergence history for the fitness value is shown in Figure 10, comparing the efficiency of different deterministic (gradient search and pattern search) and stochastic (particle swarm) optimization methods. Each optimization algorithm starts with the same initial point; however, the particle swarm algorithm is a population based method so it also includes many alternative initial

points sampled randomly from within the feasible domain. On a standard laptop computer, a single function evaluation (i.e. a complete static analysis) by the Co-Blade code can be completed in approximately 1 second.

$$f(\vec{x}_{struct}) = w * m_{blade} + \sum_{i=1}^8 \max\{1, p_i\}^2 \quad (3.1)$$

$$p_1 = \frac{\sigma_{11,max}}{\sigma_{11,FT}}$$

$$p_2 = \frac{\sigma_{11,min}}{\sigma_{11,FC}}$$

$$p_3 = \frac{\sigma_{22,max}}{\sigma_{22,FT}}$$

$$p_4 = \frac{\sigma_{22,min}}{\sigma_{22,FC}}$$

$$p_5 = \frac{|\tau_{12}|_{max}}{\tau_{12,y}}$$

$$p_6 = \left(\frac{\sigma_{zz}}{\sigma_{buckle}} \right)^\alpha + \left(\frac{\tau_{zs}}{\tau_{buckle}} \right)^\beta$$

$$p_7 = \frac{\delta_{tip}}{\delta_{tip,allowable}}$$

$$p_8 = \max \left\{ \frac{\Delta_{\omega,min}}{|\omega_m - \omega_{rotor}|} \right\}$$

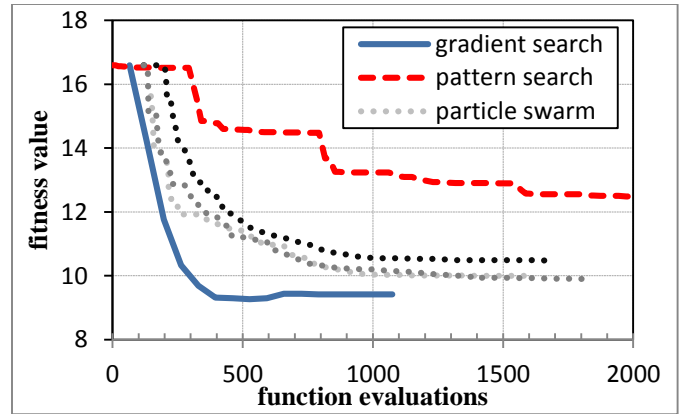


Figure 10. Comparison of convergence histories during the structural optimization for gradient search, pattern search, and particle swarm optimization algorithms. The dotted lines show 3 realizations of the stochastic particle swarm algorithm.

Initially the blade mass started at 731 kg (in air) and was reduced to 428 kg, 556 kg, and 489 kg by the gradient search, pattern search, and particle swarm algorithms respectively. The gradient search algorithm converged most quickly and found the best overall solution; however, it is very sensitive to the initial guess since it is not a global optimization algorithm. Furthermore, it is not guaranteed to satisfy the bounds and linear inequality constraints on the design variables which can occasionally produce impracticable blade designs (making this algorithm more difficult to use). The particle swarm and pattern search algorithms are

global optimization algorithms and are less sensitive to the initial points and numerous constraints on the design variables. The particle swarm algorithm performs similarly to the gradient search algorithm, and multiple realizations of the stochastic particle swarm algorithm show that it performs consistently well. The converged blade designs obtained by the gradient search and particle swarm algorithms satisfy all of the design criteria—all the constraints on maximum allowable stresses, blade tip deflection, buckling stresses, and placement of blade natural frequencies are satisfied (penalty factors $p_1 - p_8$ are less than unity).

The pattern search algorithm performs worse than the other two algorithms and one of the design criteria is not satisfied upon convergence (p_2). However, it is more instructive to continue our discussion in relation to this “failed” blade design. Figure 11 visualizes stresses within different composite layers of the blade obtained by the pattern search algorithm. Despite having the greatest strength, the NCT307-D1-34-600 carbon fiber exceeded its failure stress, which was predicted to fail in compression on the outboard region of the top surface of the blade—see Figure 11. As mentioned in the preceding paragraph, a superior optimization algorithm can create a blade which meets all the design criteria. However, the failure of the carbon fiber spar cap could also be aggravated by constraints imposed by the hydrodynamic design of the blade—which is very thin in the outboard regions of the blade due to a small chord and thin hydrofoil profile. In this thin region of the blade there is little space in the blade interior to further increase the thickness of the carbon fiber layers. Failure of the spar-cap could have possibly been avoided by selecting a thicker family of hydrofoils for the hydrodynamic design of the blade—a decision made prior to the structural optimization phase. This emphasizes the importance of coupling the hydrodynamic and structural design of the blade in order to satisfy all design criteria.

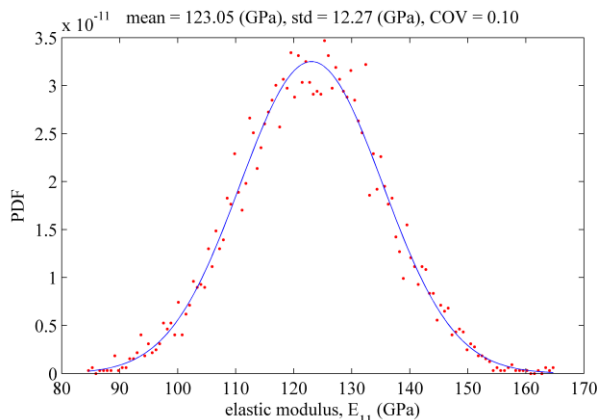


Figure 12. The composite material properties E_{11} , E_{22} , G_{12} , ν_{12} , and ρ were given a similar random variation corresponding to a normal distribution with $COV = 0.10$.

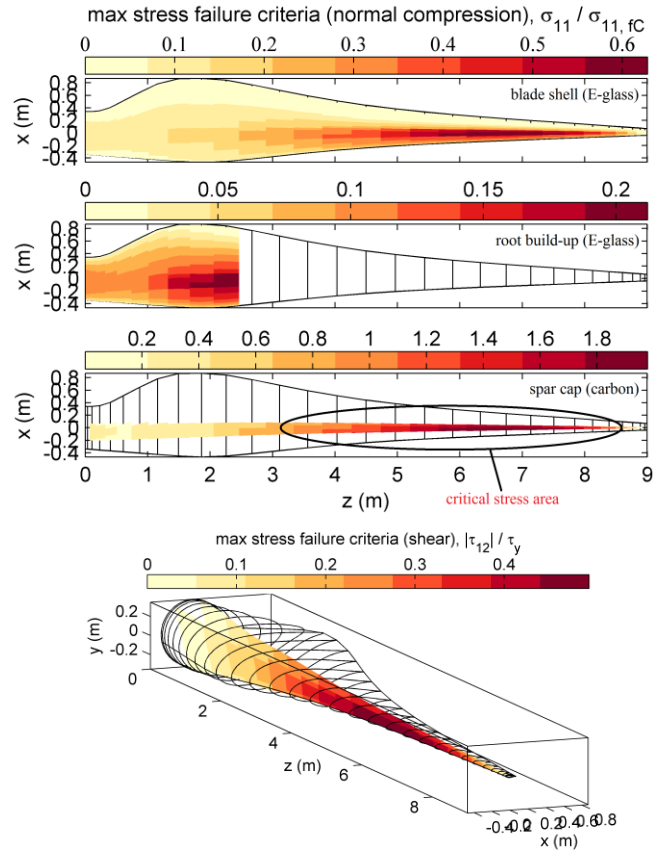


Figure 11. The “optimized” blade found by the pattern search algorithm. We visualize stresses in multiple layers of the composite blade, showing max stress failure criteria in: (a) the E-glass “blade-shell” material covering the exterior top surface of the blade, (b) the E-glass “root build-up” material, which lies directly under the “blade-shell” material, (c) the carbon fiber “spar cap” material, which lies directly under the “blade-root” material, and (d) the E-glass material on the exterior surfaces of the shear webs. A value greater than 1 indicates that the material exceeded its failure stress.

IV. EFFECTS OF UNCERTAIN MATERIAL PROPERTIES

The analysis and optimization methodology described in the previous sections assumed deterministic values of the material properties. In order to quantify the effect that uncertain material properties can have on blade response and predict overall reliability in a probabilistic design space, we consider that the material properties E_{11} , E_{22} , G_{12} , ν_{12} , and ρ listed in Table 1 actually represent the mean values of a normal distribution with a $COV = 0.10$ (for example, as shown in Figure 12). We generated 2,000 random combinations of the stochastic material properties, and then analyzed the stochastic response of the blade to predict the probability that various failure modes would occur. Only the material properties varied, and all geometric properties of the blade (e.g. twist, chord, ply thickness, ply angle, etc.) and applied hydrodynamic loads remained constant. In addition, body forces also vary since they are dependent on material density.

We continue this discussion with respect to the “optimized” blade found by the pattern search algorithm. As mentioned previously, this particular blade design exceeded its allowable stress in the carbon fiber spar cap (Figure 11). Furthermore, a number of additional failure modes are predicted to occur when the material properties have a random variation, as shown in Figure 13. Figure 13 shows the resulting variation of the penalty factors $p_1 - p_6$ which indicate the probability of exceeding allowable stresses and buckling—the solid lines in the figure represent a best fit normal distribution to each data series. As shown in Figure 13, the probability of each failure mode occurring is equal to the area under these curves, for the domain $p_i \geq 1$. From Figure 13, we can conclude that the probability of each failure mode occurring is:

- **100%** for exceeding allowable compressive stress in the carbon fiber spar cap
- **18%** for exceeding allowable tensile stress in the E-glass blade shell
- **46%** for buckling to occur in the LEP
- **73%** for buckling to occur in the TEP
- **14%** for buckling to occur in the blade tip
- **0%** for all other failure modes

By utilizing the Pearson product-moment coefficient (Eqn. 4.1), we can determine which composite material properties have the most important effects on blade response. The Pearson product-moment coefficient, defined as

$$\rho_{X,Y} = \text{corr}(X,Y) = \frac{\text{cov}(X,Y)}{\sigma_X \sigma_Y} \quad (4.1)$$

indicates the degree of linear dependence between the variables. As the Pearson coefficient approaches zero there is less of a relationship (closer to uncorrelated), and the closer the coefficient is to either -1 or 1 , the stronger the correlation between the variables. As Figure 14 shows, E_{11} and G_{12} have the largest effect on material stresses within the different components of the composite blade, and loading/unloading of the spar cap, blade shell, and shear webs are most sensitive to these variables. This type of information can provide further insight on how to optimize the composite blade. Further analysis of Figure 14 reveals that the core materials in the spar, LEP, TEP, and webs have an insignificant effect on the buckling strength of the blade, and perhaps costs can be reduced by completely removing these materials for this blade type and size.

Factors such as material corrosion, biofouling, and manufacturing process can lead to unexpected performance or premature failure of the turbine. Quantifying the effect that material uncertainties have on blade performance can inform the design of more

cost effective turbines. Although the blade cost represents only a fraction of the total cost of a wind/hydrokinetic turbine system, the blades also play the primary role in transferring loads into other sub-components of the turbine—meaning that the sizing and cost of many sub-systems are tightly coupled to the performance of the rotor blades. Inappropriate factors of safety can lead to either over-design or under-design of the device, resulting in higher cost, unexpected performance, or failure of the turbine. The analysis presented in this section can help optimize such factors of safety in order to achieve more reliable and cost effective designs.

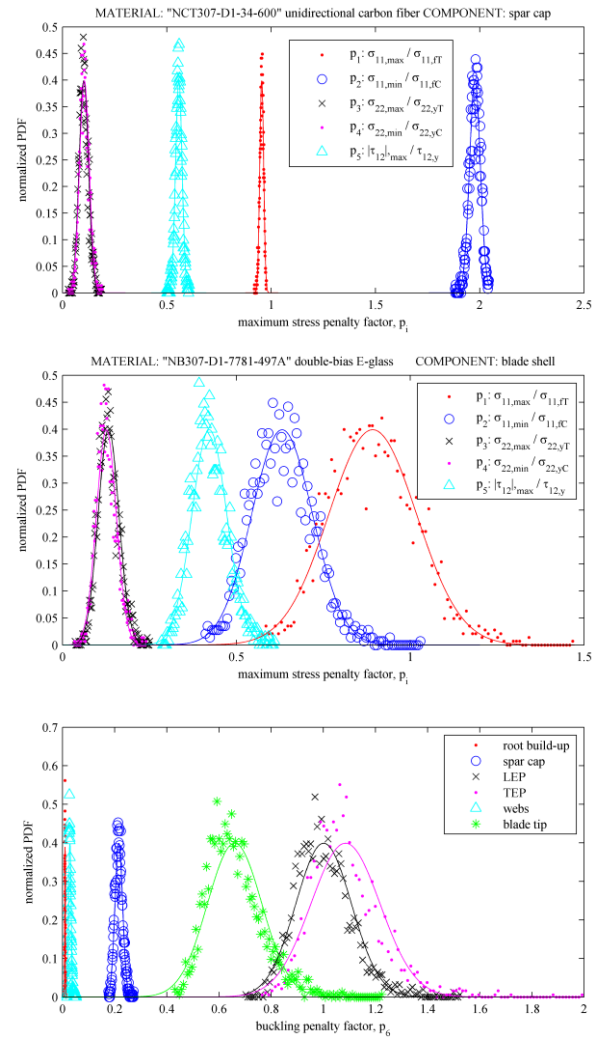


Figure 13. Normalized probability density functions¹ (PDFs) of blade response due to random variation of material properties. Figures (a) and (b) show the probability of exceeding the maximum allowable stresses in the carbon spar cap and E-glass blade shell. Figure (c) shows the probability of buckling occurring in the different components of the blade.

¹Given a probability distribution function $f(x)$, the probability that $a < x \leq b$ is $P(a < x \leq b) = \int_a^b f(x)dx$, and the normalized PDF is defined as $f(z) = \sigma f(x)$ where $z = (x - \mu)/\sigma$. μ and σ are the mean and standard deviation.

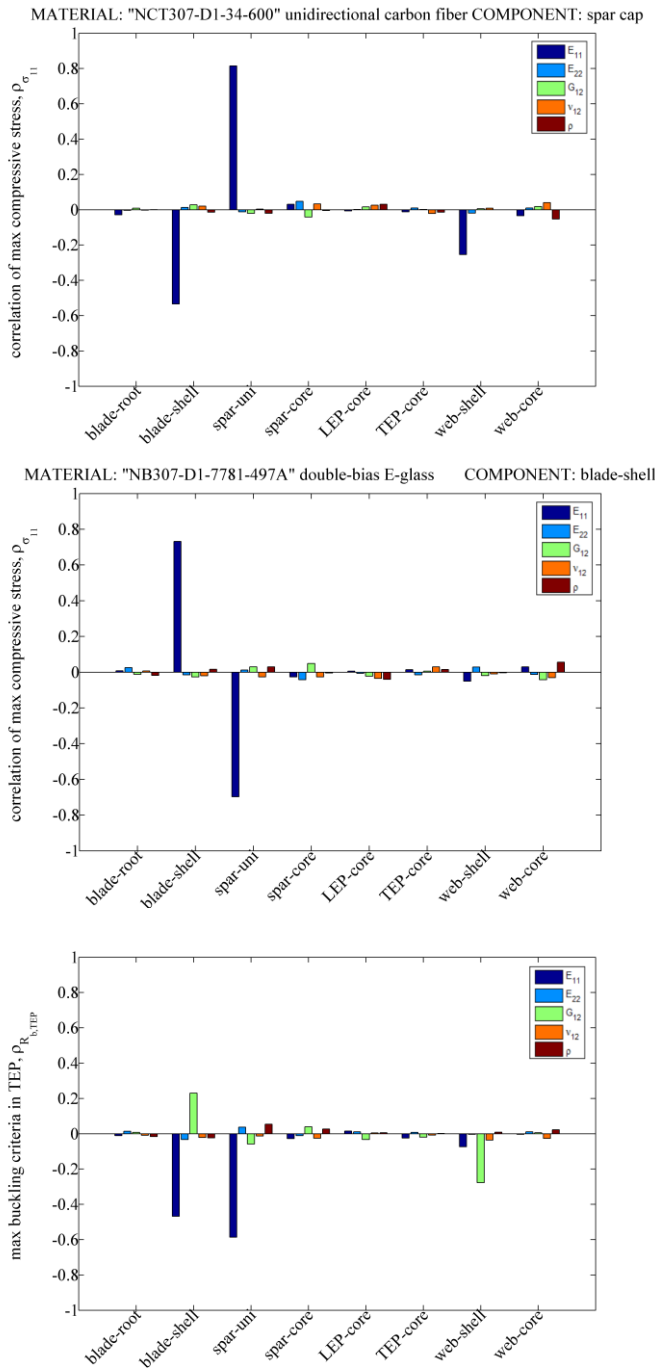


Figure 14. The Pearson product-moment coefficient showing the correlation between blade response and material properties within each component of the blade. Correlation between stress in the carbon spar caps (top), stress in the E-glass blade shell (middle), and buckling of the trailing edge panel (bottom).

V. CONCLUSION & FUTURE WORK

The present work describes the development and validation of a methodology used to design composite blades for wind and hydrokinetic turbines. An open source code, Co-Blade [1], was developed which is based upon classical lamination theory combined with an Euler-Bernoulli and shear flow theory applied to composite beams. For a limited number of composite

beam models, we have verified the efficiency and accuracy of the Co-Blade methodology compared to both analytical and finite-element analysis results. We also demonstrated an efficient structural optimization algorithm capable of minimizing blade mass while satisfying a comprehensive list of design constraints. A Monte-Carlo analysis was performed to quantify the effect of uncertain material properties on blade response which helped identify strategies to improve the performance and reduce costs of the blades.

In the future, we will also continue our validation efforts for Co-Blade by comparing to results obtained from higher resolution finite-element analysis of turbine blades with more complex composite layups. Longer term goals for this project also include coupling this structural mechanics model to an unsteady incompressible fluid solver to study the fluid-structure interactions of wind and hydrokinetic turbines.

Composite blades are susceptible to geometric, material, and loading uncertainties because of their complex configuration, manufacturing process, and dependence on fluid-structure interaction [12]. The uncertainty analysis can be extended to quantify the effects of uncertainty in material strength, blade shape, and hydrodynamic loading on blade response, safe operating envelopes, and overall reliability of composite rotors. While structural mass was used in the objective function for the structural optimization problem, more complex objective functions may provide an improved design. The idea of coupling the geometric and structural optimization of the blade was noted in Section III, with one component working as the objective and the other as a constraint. This can be helpful for optimizing the blade over the full range of expected operating conditions by optimizing the geometry of the blade for the mean expected load while simultaneously providing constraints against structural failure under off-design conditions. For only structural optimization, it may be more useful to use blade reliability as the objective function. While this is more computationally demanding, by modeling the material uncertainties and running sufficient simulations to provide an estimate of the probability of structural failure for a given design, the probability of failure can be minimized as an objective to provide optimal reliability.

ACKNOWLEDGMENTS

We thank the National Science Foundation (NSF) for providing the NSF Graduate Research Fellowship to the first author under Grant No. DGE-0718124. The first author also thanks Mark Tuttle and Brian Polagye of the University of Washington for many helpful discussions and guidance, and Hongli Jia of Hanyang University for providing the ABAQUS results for comparison.

REFERENCES

- [1] D.C. Sale. "Co-Blade: Software for Analysis and Design of Composite Blades."
<https://code.google.com/p/co-blade/>.
- [2] M. Tuttle, *Structural Analysis of Polymetric Composite Materials*, CRC Press, 2004.
- [3] O. Bauchau and J. Craig, *Structural Analysis: With Applications to Aerospace Structures*, Springer, 2009.
- [4] D. Peery and J. Azar, *Aircraft Structures*, McGraw-Hill, 2nd edition., 1982.
- [5] W. Young and R. Budynas, *Roark's Formulas for Stress and Strain*, McGraw-Hill, 7th edition, 2001.
- [6] G. Bir. NWTC Computer-Aided Engineering Tools (BModes: Software for Computing Rotating Blade Coupled Modes).
<http://wind.nrel.gov/designcodes/preprocessors/bmodes/>
- [7] J.F. Mandell, D.D. Samborsky, P. Agastra, A.T. Sears, and T.J. Wilson. "Analysis of SNL/MSU/DOE Fatigue Database Trends for Wind Turbine Blade Materials." Contractor Report SAND2010-7052, Sandia National Laboratories, Albuquerque, NM, 2010.
- [8] D.C. Sale. NWTC Computer-Aided Engineering Tools (HARP_Opt: An Optimization Code for the Design of Wind and Hydrokinetic Turbines).
http://wind.nrel.gov/designcodes/simulators/HARP_Opt/
- [9] M. G. Trudeau, "Structural and Hydrodynamic Design Optimization Enhancements with Application to Marine Hydrokinetic Turbine Blades," Master's Thesis, The Pennsylvania State University, 2011.
- [10] H. Jia, *personal communication*, Structures and Composites Laboratory, Hanyang University, Korea, 2012.
- [11] J. Thomson, B. Polagye, V. Durgesh and M. Richmond. "Measurements of Turbulence at Two Tidal Energy Sites in Puget Sound, WA." IEEE Journal of Oceanic Engineering, Vol. 37, No. 3, 2012.
- [12] M.R. Motley and Y.L. Young, "Influence of uncertainties on the response and reliability of self-adaptive composite rotors," *Composite Structures*, Vol. 94, No. 1, pp. 114-120, 2011.